The thickness of a weakly-magnetized accretion flow inside the last stable orbit of a Kerr black hole

P. Abolmasov*

Sternberg Astronomical Institute, Moscow State University, Moscow, Russia 119992

Accepted —. Received —; in original form —

ABSTRACT

If accretion disc contains weak frozen-in entangled magnetic fields, their dynamical effect may be important inside the last stable orbit because of the decompression near the sonic point. Here, I consider the radial and vertical structure of a nearly free-falling flow inside the last stable orbit of a thin disc around a Kerr black hole. The thickness of such a flow is determined primarily by the vertical stress created by radial and azimuthal magnetic fields. The thickness is predicted to oscillate vertically around its equilibrium value determined by the magnetic field balance with gravity. For thin discs, this thickness is much larger than that of the accretion disc itself. Numerical simulations with HARM2d show the vertical structure is more complicated. In particular, magnetically supported disc seems to be unstable to segregation of matter into thinner streams with the vertical scale determined by thermal pressure or other processes.

Key words: accretion, accretion discs – relativity – black hole physics – magnetic fields

1 INTRODUCTION

A thin accretion disc around a black hole ends near the innermost stable circular orbit (ISCO) radius where it becomes possible for the matter to accrete without angular momentum loss (Shapiro & Teukolsky 1983). Classical works on disc accretion usually ignore the matter inside the ISCO because the accretion proceeds on dynamical rather than viscous time scales here, and the energy dissipation is relatively low.

On the other hand, there are reasons, both observational and theoretical, for this region to become a site of intense dissipation. In particular, the sizes of X-ray emitting regions in lensed quasars (Chen et al. 2011; Morgan et al. 2012; Chen et al. 2013) seem to have sizes comparable to the last stable orbit radius, hence their fueling requires energy dissipation localized very close to the black hole. On the other hand, there are energy reservoirs that can give away some part of their energy before it is advected by the black hole. Three of them should be mentioned separately:

• Radiation trapped inside the optically thick disc. Trapped radiation is important for large accretion rates (comparable to Eddington) when the disc is hot and its optical depth high. The vertical optical depth becomes smaller near the inner edge of the disc hence the disc radiation

* E-mail: pavel.abolmasov@gmail.com

should have an additional component emitted by its innermost parts. I am not aware about any papers where this contribution was estimated, save for my work Abolmasov (2013) where the role of this radiation for rotational evolution due to radiation capture was considered.

- Magnetic fields generated and amplified in the disc. Firstly, magnetic fields are efficient in extracting the rotational energy of the black hole (Blandford & Znajek 1977; Krolik 1999). Secondly, their reconnection and dissipation due to general relativity effects, Ohmic dissipation and reconnections may heat the gas inside the ISCO up to X-ray temperatures limited primarily by inverse Compton (IC) losses (see, for instance, Pietrini & Krolik (1995)) and by the short free-fall time.
- Thermal and excess potential energy of the matter connected to disc thickness. This energy may be realized through gas heating in shock waves after the strong pressure drop near the sonic point.

All these energy sources may have luminosities about $(H/r)^2 \dot{M}c^2$, comparable to Eddington if the mass accretion rate is close to or higher than the critical (Eddington) accretion rate. For X-ray binaries, the contribution of the inner flow to the radiation emitted by the source was considered by Zhu et al. (2012) who find that up to 15% of the luminosity of the source may be emitted from inside the ISCO. Transparency and high temperatures make these parts of the accretion disc the possible source of X-rays in quasars with

the size comparable to the last stable orbit. Thus, inside the last stable orbit, there is a region of possible observational importance with the structure rarely considered in research papers.

Magnetic energy also depends on the unknown magnetization parameter $\beta = p/p_M$ (total to magnetic pressure). If the viscous stresses in the disc are connected to more or less isotropic magnetic fields, dimensionless viscosity parameter is $\alpha \sim B_r B_\varphi / 4\pi p \sim 2\beta^{-1}$. It seems a reasonable approximation to assume $\alpha\beta \gtrsim 1$.

Recent more comprehensive estimates involving three-dimensional (3D) MHD modeling argue for a somewhat smaller universal value of $\alpha\beta \simeq 0.4 \div 0.5$ (Sorathia et al. 2012). This should be borne in mind when comparing the simulation results to the real astrophysical applications. Smaller value of $\alpha\beta$ also puts slightly stronger limitations upon the approximations used in the present work (see section 6).

The ISCO sets the inner boundary of the region where a thin rotationally supported disc can exist and accretion is impossible without dissipation. In real discs, this boundary is smeared, and real discs should be transonic (in sense of radial velocity) with the slow, viscosity-driven radial creep of the accretion disc evolving into the supersonic free fall toward the horizon. Supersonic radial motion means that energy and momentum are transferred in radial direction primarily by the motion of the falling matter, and the matter itself moves nearly along the geodesics conserving its energy and angular momentum. Using the term "free fall", I refer to idealized inward motion along geodesics or to motion that is considered as such.

The standard accretion disc model (Shakura & Sunyaev 1973) is also known as the thin disc. Its vertical structure may be decoupled from the structure in radial direction. All the vertical motions are slow, and the vertical structure of the disc is determined by hydrostatic equilibrium. If the flow inside the last stable orbit preserves its disc-like geometry (its thickness is smaller than its radial extension), this approximation should probably hold. However, the vertical equilibrium needs some time to establish that implies existence of a transition region near the edge of the disc.

The structure of the transonic gas-dynamic flow near the ISCO was thoroughly considered by Beskin & Tchekhovskoy (2005). During the free-fall stage, the gas streamlines may intersect each other in one or several points (nodes) dependent on the black hole rotation parameter and initial disc thickness. A crucial feature of the transonic flow inside the ISCO is strong decompression due to the increase in radial velocity. Surface density changes by a factor of $\sim v_r^{disc}/v_K \sim \alpha(H/r)^2 \ll 1$, where H is disc thickness at radial distance R. Gas pressure decreases even stronger, at least as $\sim \left(\alpha(H/r)^2\right)^{\Gamma}$, where $\Gamma \sim 5/3$ is the adiabatic index. Moreover, the pressure in the inner parts of accretion discs often includes important contribution from radiation pressure that drops when the flow becomes optically thin 1.

All this implies that, unless the disc scale height changes by a considerable amount, the vertical structure of the disc is very far from equilibrium.

One pressure source that survives this density drop is the radial magnetic field. The other two components decrease linearly with the density drop but the radial component of magnetic field changes continuously due to flux conservation (approximately as $B^r \propto (HR)^{-1}$). If the magnetic fields are in equipartition inside the accretion disc, Maxwellian stresses $\sim B^2$ will dominate over other pressure contributions inside the ISCO. This makes the tangential (vertical) stress the primary force to balance the gravity in the free-falling region inside a thin disc and thus to influence its vertical structure. Depending on the parameter values (Kerr parameter, disc thickness and radial velocity in the disc), the vertical structure may be closer either to the free-fall solution (as in Beskin & Tchekhovskoy (2005)) or to a magnetically supported analogue of the thin accretion disc.

Apart from the radial, azimuthal magnetic field component plays important role because the magnetic field is wound up by differential rotation. As it will be shown in section 3, the azimuthal magnetic fields easily become stronger than radial. If both B^r and B^φ are present, magnetic stress may also affect momentum transfer in radial direction. This effect is ignored here but may become important if either the matter is strongly magnetized $(\alpha\beta\gg1)$ or the disc thickness is high. In section 6, I consider the limits of this approximation.

In this work, I consider the radial and vertical structure of an equatorial thin disc-like flow that has negligible gas pressure but strong enough magnetic fields to affect the vertical force balance. Radial structure is assumed to be governed by gravity only, $u^z \ll u^r \sim u^\varphi \sim u^t$.

The properties of such a flow are derived from the fundamental conservation laws (see next section). Radial structure may be simply considered as a result of energy and angular momentum conservation. Vertical structure, however, requires evaluation of the vertical gravity in the co-moving frame (see section 2.3). The role of magnetic field components is considered in section 3. The Cauchy problem for the vertical scale height is formulated and the results are presented in section 4. To check my semi-analytical results, I also compute a series of numerical two-dimensional models using the publicly available code HARM. Results of these simulations are given and compared to the simplified model in section 5. Discussion and conclusions are given in section 6.

density, $\dot{M}_{Edd}=\frac{4\pi GM}{c\varkappa_T}$ is the Eddington (critical) mass accretion rate. Hence unless accretion is significantly supercritical (Shakura & Sunyaev 1973), the inner flow has optical depth less than several.

¹ Scattering vertical optical depth of a free-falling flow is of the order of mass accretion rate in Eddington units, $\tau \simeq \varkappa_T \Sigma \sim \frac{\varkappa_T \dot{M}}{4\pi R u^T} \sim \frac{\dot{M}}{\dot{M}_{Edd}}$, where \varkappa_T is Thomson opacity, Σ is surface

2 IDEAL FLOW INSIDE THE LAST STABLE ORBIT

2.1 Basic assumptions

Let us consider the supersonic part of a thin transonic equatorial flow upon a Kerr black hole. Radial motion is practically a free fall, but for the vertical structure, both gravity and pressure gradients will be considered.

I consider Kerr metric in Boyer-Lindquist coordinates (Boyer & Lindquist 1967) t, r, φ, θ .

$$ds^{2} = -\alpha^{2}dt^{2} + \frac{\Sigma^{2}}{\rho^{2}}\sin^{2}\theta \left(d\varphi - \omega_{LT}dt\right)^{2} + \frac{\rho^{2}}{\Delta}dr^{2} + \rho^{2}d\theta^{2}$$

Here:

$$\alpha^2 = \frac{r^2 \Delta}{\Sigma^2}$$

$$\rho^2 = r^2 + a^2 \cos^2 \theta$$

$$\Sigma^2 = (r^2 + a^2)^2 - a^2 \Delta \cdot \sin^2 \theta$$

$$\Delta = r^2 - 2r + a^2$$

$$\omega_{LT} = \frac{2ar}{\Sigma^2}$$

All the calculations are performed near the equatorial plane $(\cos\theta \simeq 0)$. To calculate the vertical gravity, terms of the order $\cos^2\theta$ should be retained in metric components. Normalized dimensionless units are used GM=c=1.

In the most general form, energy-momentum conservation may be written as:

$$T^{ik}_{:k} = 0$$

Continuity equation:

$$(\rho u^i)_{:i} = 0$$

Here, energy-momentum tensor $T^{ik}=\rho u^iu^k+pg^{ik}+T^{ik}_{EM}$, and practically everywhere below the pressure term is dropped (p=0) because, as it was shown in the Introduction, magnetic tensions overwhelm thermal pressure inside the last stable orbit. The dynamical equation for a test particle may be thought of as a consequence of the above two conservation laws:

$$u^{k}u_{;k}^{i} = -\frac{1}{\rho}(T_{EM})_{;k}^{ik} - \frac{1}{\rho}p^{;i}$$

If one considers the vertical structure:

$$u^r u_{,r}^z = a_z + g_z,$$

where a_z is the acceleration created by magnetic tensions (will be considered in section 3) and thermal pressure,

and g_z is vertical gravity term (see section 2.3) responsible for the difference between covariant and partial derivatives in the above expressions. To estimate the vertical gravity, Christoffel symbols should be expanded at least to second order in $\cos\theta$. Together with θ , vertical distance z is also used, $z=r\cos\theta\ll r$. For any tensor quantity or Christoffel symbol, coordinate transformation from θ to z near equator requires multiplication (division) by the factor of $|dz/d\theta|=r$ if the quantity is contravariant (covariant) in θ . Note that the corresponding metric component is trivial $g_{zz}=g^{zz}=1$ and hence for any vector or tensor quantity evaluated near the equatorial plane upper and lower position of z index are equivalent.

2.2 Radial structure

For a particle falling free in Kerr space-time, energy $-u_t$ and angular momentum u_φ are conserved. Radial velocity can be expressed straightforward through the conserved 4-velocity components:

$$g^{ik}u_iu_k = -1$$

$$u_r \simeq \sqrt{-g_{rr}(g^{tt}u_t^2 + 2g^{\varphi t}u_tu_\varphi + g^{\varphi \varphi}u_\varphi^2 + 1)}$$
 (1)

Contravariant velocity component may be calculated as $u^r = g^{rr}u_r$.

2.3 Vertical acceleration

Vertical acceleration as measured in the co-moving frame:

$$a_z = u^k u_{z,k} = u^k \times \left(u_{z,k} - \Gamma^l_{zk} u_l \right)$$

Since the flow is one-dimensional (we neglect vertical motions with respect to radial), this relation may be rewritten as:

$$u_{z,r} = \frac{1}{u^r} \left(a_z + \Gamma_{lzk} u^l u^k \right)$$

where $g_z = \Gamma_{lzk} u^l u^k$ is vertical gravity. Motion along a geodesic corresponds to $a_z = 0$, while in a more general case a_z may be connected to some external force.

$$\begin{split} g_z &= \Gamma_{rzr} \left(g^{rr}\right)^2 u_r^2 + \Gamma_{zt}^t u^t u_t + \Gamma_{zt}^\varphi u^t u_\varphi + \Gamma_{z\varphi}^t u^\varphi u_t + \Gamma_{z\varphi}^\varphi u^\varphi u_\varphi = \\ &= \Gamma_{rzr} g^{rr} u_r^2 + \left(\Gamma_{tzt} (g^{tt})^2 + 2\Gamma_{\varphi zt} g^{\varphi t} g^{tt} + \Gamma_{\varphi z\varphi} (g^{\varphi t})^2\right) u_t^2 + \\ &+ \left(\Gamma_{tzt} (g^{\varphi t})^2 + 2\Gamma_{\varphi zt} g^{\varphi t} g^{\varphi \varphi} + \Gamma_{\varphi z\varphi} (g^{\varphi \varphi})^2\right) u_\varphi^2 + \\ &+ \left(\Gamma_{tzt} g^{\varphi t} g^{tt} + \Gamma_{\varphi zt} \left((g^{\varphi t})^2 + g^{tt} g^{\varphi \varphi}\right) + \Gamma_{\varphi z\varphi} g^{\varphi \varphi} g^{\varphi t}\right) u_t u_\varphi \end{split}$$

If u^r is substituted following (1):

$$g_z = u_\varphi^2 \left(g^{\varphi\varphi} \Gamma_{z\varphi}^\varphi + g^{\varphi t} \Gamma_{zt}^\varphi - g^{\varphi\varphi} \Gamma_{zr}^r \right) + u_\varphi u_t \left(g^{tt} \Gamma_{z\varphi}^\varphi + g^{\varphi t} \times \left(\Gamma_{z\varphi}^\varphi + \Gamma_{zt}^t - 2\Gamma_{zr}^r \right) + g^{\varphi\varphi} \Gamma_{z\varphi}^t \right) + u_z^2 \left(g^{tt} \Gamma_{zt}^t + g^{\varphi t} \Gamma_{z\varphi}^t - g^{tt} \Gamma_{zr}^r \right) - \Gamma_{rz}^r$$

Relevant metric components and Christoffel symbols evaluated near z=0 (leading terms in z/r retained) are equal:

$$g^{tt} = -\frac{1}{r\Lambda} \left(r^3 + a^2(r+2) \right)$$

$$g^{\varphi\varphi} = \frac{r-2}{r\Lambda}$$

$$g^{\varphi t} = -\frac{2a}{r\Delta},$$

where $\Delta = r^2 + a^2 - 2r$.

$$\Gamma_{rzr} = \frac{a^2}{r^2 \Delta} z$$

$$\Gamma_{\varphi z\varphi} = -\left(1 + \frac{a^2(r^3 + 4r^2 + 2a^2)}{r^5}\right)z$$

$$\Gamma_{\varphi zt} = \frac{2a(r^2 + a^2)}{r^5} z$$

$$\Gamma_{tzt} = -\frac{2a^2}{r^5}z$$

$$\Gamma^r_{zr} = \frac{a^2}{r^4} z$$

$$\Gamma_{z\varphi}^{\varphi} = -\frac{r^3 + 2a^2}{r^5}z$$

$$\Gamma_{zt}^t = \frac{2a^2}{r^5}z$$

$$\Gamma^{\varphi}_{zt} = \frac{2a}{r^5} z$$

$$\Gamma_{z\varphi}^t = -\frac{2a^3}{r^5}z$$

Since all the Christoffel symbols are proportional to z, one may rewrite the expression for the vertical acceleration as:

$$g_z = -\Omega_z^2(r, a)z \tag{2}$$

where $\Omega_z(r,a)$ is the local co-moving frequency of vertical oscillations. Following Abramowicz et al. (1997), one can substitute the above expressions for Christoffel symbols and metric components and express Ω_z in the compact and elegant form independent of radial velocity:

$$\Omega_z^2 = \frac{1}{r^4} \left(u_\varphi^2 - a^2 \left(u_t^2 - 1 \right) \right) \tag{3}$$

3 ACCELERATION CAUSED BY MAGNETIC FIELD TENSION

3.1 Magnetic field components

Let us consider the case of ideal electrodynamics where the electric field is exactly zero in the comoving frame and thus $u_k F^{ik} = 0$, where F^{ik} is electromagnetic tensor. Electromagnetic fields in this case may be described solely by one co-moving magnetic field four-vector B^i , $B^i = u_k *F^{ik}$, where $*F^{ik} = e^{ikjl}F_{jl}$ is dual electromagnetic tensor. Such description was used, for example, in Krolik (1999); Komissarov (2006). The dual tensor itself may be expressed as $*F^{ik} = u^i B^k - u^k B^i$. It may be shown that the scalar product $u_i B^i = 0$ meaning that the magnetic field has zero temporal component in the co-moving frame. As long as $u_z \ll u_r \sim u_\varphi \sim u_t$, one can safely neglect the vertical components of the field when expressing the temporal component $B^t = -\frac{1}{u_t} \left(u_r B^r + u_\varphi B^\varphi \right)$.

The first pair of Maxwell equations may be written as (see for example Landau & Lifshitz (1971), chapter IV):

$$({}^*F^{ik})_{;k} = 0,$$

or, since the tensor is antisymmetric (ibid., chapter X):

$$\left(\sqrt{-g} \times^* F^{ik}\right)_k = 0,$$

where $\sqrt{-g} \simeq r^2$ near the equator. Integrating over the solid angle (θ and φ coordinates) and taking into account the considered configuration should be axisymmetric and stationary yields the following system of invariants:

$$4\pi Hr\left(u^i B^r - u^r B^i\right) = \Phi^{ri},\tag{4}$$

It is assumed that dynamically important magnetic fields are concentrated inside the accretion flow of thickness H. Since magnetic fields are advected by accreting matter one should not expect to find strong magnetic fields far from the equatorial plane. Radial magnetic field is easily obtained by contracting (4) with 4-velocity, bearing in mind that u_t and u_{φ} are constant and radial motions near the edge of the disc are negligible.

$$B^r(r) = \frac{H_0 r_0}{H r} B_0^r \tag{5}$$

Let us first consider magnetic field that is purely poloidal in the disc. Then, substitution of $i=\varphi$ into (4) yields:

$$B^{\varphi}(r) = \frac{H_0 r_0}{H r u^r} \times \left[u_0^r B_0^{\varphi} + \left(u^{\varphi} - u_0^{\varphi} \right) B_0^r \right] =$$

$$= \frac{H_0 r_0}{H r} \times \frac{u^{\varphi} - u_0^{\varphi}}{u^r} B_0^r$$
(6)

Hence for the temporal component:

$$B^{t}(r) = -\frac{H_{0}r_{0}}{Hru^{r}u_{t}} \times \left[(u_{r}u^{r} + u_{\varphi}(u^{\varphi} - u_{0}^{\varphi})) B_{0}^{r} + u_{0}^{r}u_{\varphi}B_{0}^{\varphi} \right] =$$

$$= -\frac{H_{0}r_{0}}{Hr} \times \frac{u_{r}u^{r} + u_{\varphi}(u^{\varphi} - u_{0}^{\varphi})}{u^{r}u_{t}}B_{0}^{r}$$
(7)

Approximately, these equalities work well whenever we are far enough from the disc edge. Note that initial toroidal field enters the above expressions in combination $u_0^r B_0^{\varphi}$ hence one may adopt $B_0^{\varphi} \simeq 0$ as well as $B_0^z \simeq 0$ since:

$$B^z(r) = \frac{H_0 r_0 u_0^r}{H r u^r} \times B_0^z \tag{8}$$

It is natural to assume that near the ISCO, magnetic field components are of the same order of magnitude, $\sqrt{g_{\varphi\varphi}}B^{\varphi}\sim\sqrt{g_{rr}}B^{r}$, while the radial velocity is much smaller than the azimuthal. Further inside, where $u^{\hat{\varphi}}\sim u^{\hat{r}}$, azimuthal field becomes much larger and $B^{\varphi}\sim\frac{u^{\varphi}}{u^{r}}B^{r}$. Azimuthal field behaves reasonable near the ISCO since the square bracket in (6) approaches zero when $r\to r_{ISCO}$. This azimuthal field may be considered wound up by differential rotation.

It is however instructive to consider the opposite case when initial toroidal fields dominate. If initially radial magnetic field $B_0^r = 0$, radial magnetic fields are also absent at smaller radii ($B^r = 0$), and azimuthal and temporal components of initially purely toroidal field equal:

$$B_{tor}^{\varphi} = \frac{H_0 r_0}{H r} \frac{u_0^r}{u^r} B_0^{\varphi} \tag{9}$$

$$B_{tor}^{t} = -\frac{H_{0}r_{0}}{Hr} \frac{u_{0}^{r}}{u^{r}} \frac{u_{\varphi}}{u_{t}} B_{0}^{\varphi}$$
 (10)

In this case, the magnetic field strength is proportional to the initial radial velocity and is thus important either in thicker discs or when toroidal fields are much stronger than poloidal. Two-dimensional simulations suggest that magnetic fields in the disc do have such anisotropy, see section 5.2.

3.1.1 Seed fields in the disc

To estimate the initial magnetic field for the important case of standard disc, one can adopt equipartition in the form $p_{M0} = p_0/\beta$, where p_0 is the characteristic value of standard disc pressure near the ISCO:

$$p_{M0}/\dot{M} \simeq \frac{3}{8\pi\alpha\beta} \frac{\Omega_K^0}{H_0} \tag{11}$$

Assuming the field isotropic, one can obtain an estimate for the radial field in all the standard disc regimes:

$$B_0^{\hat{r}} \simeq \sqrt{\frac{\Omega_K^0 \dot{M}}{\alpha \beta H_0}} \tag{12}$$

This estimate will be used later for numerical calculations. Since the acceleration created by magnetic fields $a_B \propto B^2/\dot{M}$ (see next sub-section), this result is quite universal and does not directly depend on \dot{M} . Physical component of B_0^z is expected to be of the same order, but since the impact of the vertical fields is diminished by the flow rarefaction, in numerical calculations I neglect vertical fields.

3.2 Vertical acceleration

As it was shown in section 2.1, the motion of a test particle at the surface of the flow is determined by vertical gravity and magnetic stress. Let us leave only two constituents in $T^{ik} \simeq \rho u^i u^k + T^{ik}_{EM}$ and assume the electromagnetic part of the stress-energy tensor has only one component T^{zz}_{EM} important for the vertical structure of the disc equal to:

$$4\pi T_{EM\ z}^{z} = F^{zj} F_{jz} - \frac{1}{4} F^{ik} F_{ik} =$$

$$= \frac{1}{2} \left(B^{2} - 2B_{z}^{2} \right) = \frac{1}{2} \left(B_{r} B^{r} + B_{\varphi} B^{\varphi} + B_{t} B^{t} - B_{z} B^{z} \right)$$

Or, using physical magnetic field components:

$$-4\pi T_{EM\ z}^{z} = \frac{1}{2} \left(B_{\hat{\varphi}}^{2} + B_{\hat{r}}^{2} + B_{\hat{t}}^{2} - B_{\hat{z}}^{2} \right) \tag{13}$$

Vertical acceleration due to magnetic pressure (vertical gradient here is approximated as $d/dz \simeq 1/H$):

$$a_B^z = u^k u_{;k}^z \simeq \frac{1}{\rho} \frac{d}{dz} (T_{EM\ z}^z) \simeq -\frac{4\pi T_z^z r u^r}{\dot{M}}$$
 (14)

where the energy-stress tensor component is estimated by the above equation (13), and the magnetic field component values are calculated following the equations (5-7) or (9-10) of the previous sub-section.

3.3 Equilibrium disc thickness

3.3.1 Magnetically supported disc

The condition of vertical equilibrium may be written as:

$$a_B^z = -g_z$$

Above we have seen (equation (2)) that $g_z \propto z$. Magnetic field acceleration, on the other hand, is proportional to compression factor squared $\propto (H_0/H)^2$, with a coefficient depending on r and a and initial fields. This may be written as:

$$\Omega_z^2(r,a)H = \frac{K(r,a)}{\alpha\beta} \frac{H_0}{H^2},$$

where K(r,a) is a certain function of radius and Kerr parameter.

$$H_{eq} = \left(\frac{H_0 K(r, a)}{\alpha \beta \Omega_z^2(r, a)}\right)^{1/3} \tag{15}$$

Highly dissipative flow will have a disc half-thickness close to the equilibrium vertical scale H_{eq} , otherwise it will oscillate near this value (see below section 4.4).

Scaling $H_{eq} \propto H_0^{1/3}$ suggests that for a disc thin enough, $H_{eq} > H_0$ and the inner flow of a thin disc should be comparably geometrically thick. It should be also noted that $a_B^z \propto \beta^{-1}$ hence $H_{eq} \propto \beta^{-1/3}$. On the other hand, for relatively thick discs, high $\alpha\beta \gg 1$ are needed to prevent the disc height exceeding r hence I restrict myself to the very large value of $\beta=100$ when solving the equations numerically.

3.3.2 Thermal pressure

If vertical gravity can not be balanced by magnetic fields, the free fall in vertical direction is stopped by increasing pressure of the compressed gas. For small enough rotation parameters and initial radial velocities, the radial free-fall times are long enough to approach the equilibrium state when:

$$\Omega_z^2 H_m \simeq \frac{p_c}{\rho_c H_m},$$

where ρ_c and p_c are density and pressure near the equatorial plane, and H_m is the vertical scale,

$$H_m \simeq \sqrt{\frac{p_c}{\rho_c}} \Omega_z^{-1} \tag{16}$$

Pressure and density here are determined by compression and decompression processes in the flow as well as by losses to radiation that should be important in reality but are not included in the simulations presented below (section 5) in this work.

4 NUMERICAL SOLUTION

4.1 The Cauchy problem

Let us consider a free-falling inner disc with a density independent of vertical coordinate in the range -H < z < H. Such a disc would preserve its vertical structure, and its evolution with time (and r) is self-similar in the sense that all the particle trajectories differ only in some multiplication factor in vertical direction. Vertical four-velocity component u^z is thus proportional to z, and it is sufficient to consider the motion of the particles consisting the surface of the inner disc (z = H). The thickness itself is $H = \int u^z d\tau$. Thickness as a function of radius obeys the equation:

$$u^{r}\frac{d}{dr}\left(u^{r}\frac{dH}{dr}\right) = g_{z} + a_{B} \tag{17}$$

where the accelerations g_z and a_B are calculated according to equations (2) and (14), respectively. Solution is obtained by solving the Cauchy problem for this equation where all the coefficients depend on r and H. The initial conditions are $H(r_{ISCO}) = H_0$ and $dH/dr(r_{ISCO}) = 0$.

For the two right-hand terms in (17), scalings with disc height are different: $g_z \propto H$ and $a_B \propto H^{-2}$. At each radius value, there is an equilibrium thickness (see section 3.3), and the solution of the above equation in general case is oscillating around the equilibrium value. Oscillation frequency is set mainly by the gravity term and is thus close to $\Omega_z(r,a)$. Velocity components u_φ and u_t are assumed constant and equal to the values at the last stable orbit, and u^r is estimated using the normalization condition $(u_i u^i = -1)$ modified to make the evolution near the disc boundary smoother:

$$u_r(r) \simeq \sqrt{-g_{rr}(g^{tt}u_t^2 + 2g^{\varphi t}u_tu_\varphi + g^{\varphi \varphi}u_\varphi^2 + 1) + u_{\hat{r},0}^2},$$
(18)

where $u_{\hat{r},0}$ is the physical radial velocity at the ISCO

that was estimated (unless otherwise stated) according to the non-relativistic thin disc model as:

$$u_{\hat{r},0} \simeq v_r \simeq \alpha \frac{H_0^2}{r_0} \Omega_K^0$$

Far enough from ISCO, the flow is independent of the exact value of initial radial velocity, especially if it is small. At ISCO, corrections to energy and momentum due to nonzero radial velocity are quadratic in $u_{\hat{\tau},0}$ and may be generally ignored.

4.2 Ballistic trajectories

If no pressure sources are present and the trajectories are allowed to intersect each other, one arrives to the case considered by Beskin & Tchekhovskoy (2005). The flow intersects itself at certain distances, and the number of nodes decreases with Kerr parameter and initial radial velocity. Positions of the three innermost nodes are shown in figure 1 for $u_{r,0} = 0$.

Adding small magnetic field or other pressure source transforms the nodes into shocks with Mach numbers essentially close to unity because the vertical motions are expected to stop when $p \simeq \rho v_z^2$ where p includes both magnetic and thermal pressure in vertical direction.

4.3 Equilibrium disc height

As it was shown in section 3.3, equilibrium disc thickness scales $\propto (h_0/\alpha\beta)^{1/3}$, where $h_0 = H_0/r_0$ is relative initial half-thickness of the disc. The equilibrium quantity H_{eq} is a function of radius with a maximum at $R \sim 0.85 r_{ISCO}$, weakly dependent on Kerr parameter (see figure 2). Equilibrium thicknesses at different radii as functions of Kerr parameter are shown in figures 3 and 4, correspondingly. Relative disc thickness $h_{eq} = H_{eq}/r$ is a much weaker function of a.

If seed magnetic fields are primarily poloidal, numerical results allow to make the following estimate for the equilibrium disc thickness near r_{ISCO} , slightly dependent on a:

$$h_{eq, out, pol} \simeq (0.2 \div 0.3) \left(\frac{h_0}{\alpha \beta}\right)^{1/3}$$
 (19)

Near the horizon, a similar estimate may be made:

$$h_{eq, in, pol} \simeq (0.35 \div 0.6) \left(\frac{h_0}{\alpha \beta}\right)^{1/3}$$
 (20)

Equilibrium relative disc thickness at intermediate radii is much closer to the estimate at the horizon, as one can see in figure 3.

If toroidal fields dominate in the accretion disc and thus determine the structure of the flow inside the ISCO, the equilibrium thickness approaches zero when $a \to 1$ and $r \to r_{hor}$ (see figure 2). For relatively low $a \lesssim 0.7$ and for counterrotation, initial thickness of the flow supported by toroidal fields is:

$$h_{eq, out, tor} \simeq (0.7 \div 0.8) \left(\frac{h_0 (u_0^{\hat{r}})^2}{\alpha \beta}\right)^{1/3}$$
 (21)

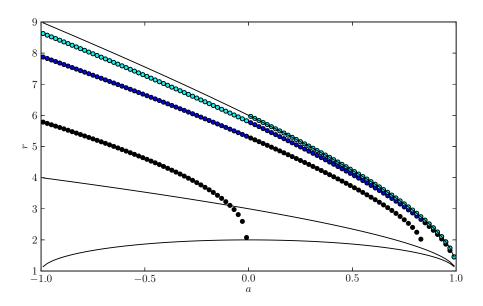


Figure 1. Innermost three nodes of ballistic (free-falling) solutions as functions of Kerr parameter. Characteristic radii are shown with solid curves: horizon r_{hor} (the smallest), photon circular orbit radius r_{ph} and last stable orbit radius r_{ISCO} (the largest).

If the initial toroidal fields are large, this formula is a reasonable estimate for the initial thickness, but to support the inner parts of the flow one needs to consider seed radial fields.

4.4 Height oscillations

Clearly, equation (17) describes disc thickness oscillations and has one neutral focus near $H=H_{eq}$. If vertical motions are subject to any kind of dissipation (shock waves, bulk viscosity etc.), the oscillations are damped. In figure 5, disc thickness oscillations with radius are shown for different Kerr parameters. Self-intersecting dust free-fall solutions are shown with dots, and dashes mark the equilibrium disc thickness. Rapid oscillations near the ISCO occur only for smaller initial radial velocities.

5 NUMERICAL SIMULATIONS IN 2D

5.1 Basic information and code setup

HARM is a publicly available code that allows to consider MHD problems in full General Relativity in a fixed Kerr background metric (Gammie et al. 2003; Noble et al. 2006). It was successfully applied to problems like Blandford-Znajek magnetosphere structure and jet formation, magneto-rotational instability development in accretion discs and tori and some others. It does not include implicitly any dissipation mechanisms such as magnetic recon-

nections and fluid viscosity but they effectively emerge at small spatial scales due to numerical viscosity. Radiation is neither included in the code hence a viscous disc conserves its thickness and does not evolve toward the thin disc solution.

Currently, there is fair understanding of what happens to a regular vertical magnetic field frozen into a thick disc (see for example Penna et al. (2010)). Black hole then becomes immersed in a regular magnetic field with the strength determined by flux accumulation. If magnetic field instead is chaotic and its spatial scales are small enough, the strength of regular fields through the black hole horizon are smaller than that of the fields in the inner disc and accretion flow. The critical correlation length may be estimated by comparing the regular and chaotic magnetic field components near the horizon, B^{reg} and B^{ch} , where:

$$B^{reg} \simeq \frac{\Phi}{\pi r_0^2} \simeq B_0 \times \frac{L_{reg}^2}{r_0^2},$$

where L_{reg} is characteristic magnetic field correlation scale in the disc, and:

$$B^{ch} \simeq \frac{H_0 r_0}{H_{in} r_{in}} B_0$$

Regular field dominates if the fields in the inner parts of the accretion disc are correlated on spatial scales about of larger than:

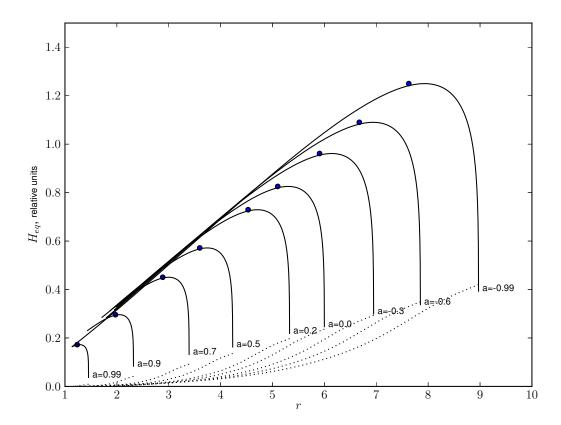


Figure 2. Equilibrium disc thicknesses for different values of Kerr parameter. In this graph, $\alpha\beta = 100$ and $h_0 = 0.1$ is assumed. Solid and dotted lines correspond to radial and toroidal seed magnetic fields.

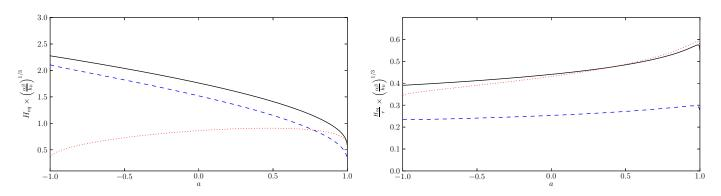


Figure 3. Normalized equilibrium disc thicknesses as a function of Kerr parameter at three characteristic radii: midway between r_{ISCO} and horizon (solid line), near r_{ISCO} (blue/dashed) and near r_{hor} (red/dotted). Again, $\alpha\beta = 100$ and $h_0 = 0.1$ is assumed. The left panel shows absolute, and the right relative thicknesses. Purely radial seed fields were considered.

$$L_{reg} \sim \sqrt{\frac{H_0 r_0^3}{H_{in} r_{in}}} \gtrsim r_0 \tag{22}$$

Here, the "zero" index corresponds to the last stable orbit, and "in" to the quantities near the horizon.

To check the viability of the analytical approach to the inner flow, I formulate a series of two-dimensional HARM

problems with the following initial conditions. Initially, an aligned torus orbiting a rotating black hole was placed between the last stable orbit and approximately $50GM/c^2.$ Exact solution of Fishbone & Moncrief (1976) was chosen, one of the standard and well-tested forms of initial matter distribution. Torus size parameters were chosen depending on the Kerr parameter (see table 1), and \varkappa parameter was everywhere set to 1.

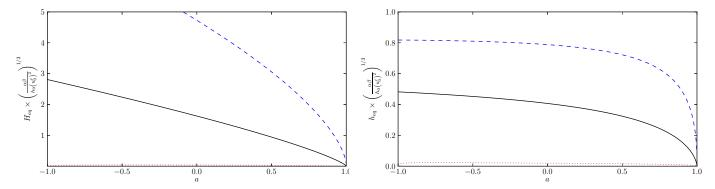


Figure 4. Same as previous figure, but initially toroidal seed fields were considered instead of radial. Dotted curve was calculated for the radial coordinate equal to $1.05r_{hor}$.

Poloidal initial magnetic fields were set through vector potential having only one (azimuthal) non-zero component A_{φ} :

$$\boldsymbol{B}_{nol} = \nabla \times \boldsymbol{A}$$

$$B^r = -\frac{1}{\sqrt{-q}} \frac{\partial A_{\varphi}}{\partial \theta}$$

$$B^{\theta} = -\frac{1}{\sqrt{-g}} \frac{\partial A_{\varphi}}{\partial r},$$

where $g = -\rho^4 \sin^2 \theta = -(r^2 + a^2 \cos^2 \theta)^2 \sin^2 \theta$ is metric determinant.

5.1.1 Single loop case

The above estimate (22) means that even smooth seed magnetic fields with spatial gradients $\sim B/r$ produce stronger magnetic fields in the accretion flow than the regular vertical field component. Thus the first case I consider in four of the six simulation runs is a single-loop scenario with A_{φ} set proportional to the local pressure in the torus. This configuration is also standard, it was used for example in Shafee et al. (2008).

Three models A1, B1 and C1 reproduce accretion upon black holes with different Kerr parameters (see table 1 for details). Counter-rotation is described via a < 0. Dependence on resolution was considered by performing one additional simulation, B1h.

5.1.2 Multi-loop case

On the other hand, magnetic fields may be small-scale and chaotic. Stochastic poloidal field configuration may be thought of as produced by a number of toroidal currents randomly placed in the disc. Vector potential produced by such a current in the non-relativistic case is given by the following expression:

$$A_{\varphi}^{loop} \propto \sqrt{\frac{r_{loop}}{r}} \times \left(\left(\frac{2}{k} - k\right) \mathbf{K}(k) - \frac{2}{k} \mathbf{E}(k) \right),$$

where

$$k^{2} = \frac{4r_{loop}r}{(r + r_{loop})^{2} + (z - z_{loop})^{2}}$$

and E(k) and K(k) are complete elliptic integrals of the first and the second kind (this solution is given, for example, in Batygin & Toptygin (1978)). Though the solution for a single current loop is not exact in general relativity, it corresponds to some current configuration not too much different from a single loop. The worst disadvantage of this solution is that it creates magnetic stresses that are far from proportionality with the gas energy and momentum density. To soften this effect, infinitely-thin loops were replaced by flux "tubes" with vector potential multiplied by the factor:

$$A_{\varphi}^{tube} = A_{\varphi}^{loop} \times \frac{d}{\sqrt{1+d^4}},$$

where
$$d = \sqrt{(r - r_{loop})^2 + (z - z_{loop})^2}$$
.

Poloidal magnetic fields were set as a sum of 50 toroidal current tubes with random current scaling with the local gas pressure and randomly placed inside the torus. The two simulation runs differ in symmetry: in one case (A50s), vector potential was made symmetrical with respect to the orbital plane, in the other case anti-symmetrical.

In both scenarios, the fields were scaled proportional to the local gas pressure with the initial $\beta=2000$. I set no initial toroidal fields since poloidal fields are rapidly (on the time scales of several GM/c^2) wound up and converted to toroidal.

In total, 6 simulation runs were performed with different Kerr parameter values (see table 1). Except for one run, the grid was chosen with 128 points in radial direction and 192 in polar angle that provides $\Delta\theta \sim 10^{-2}$ resolution in polar angle. One of the simulations, B1, was repeated at higher resolution (B1h has resolution 192×320 instead of 128×192).

The initial poloidal β value was set to 2000, but the magnetic fields are substantially amplified by differential rotation, turbulence and instabilities. For every run, there is an initial period when only very weakly magnetized matter is accreted, and intense accretion of the magnetized matter from the disc starts after several hundreds of GM/c^3 . All the quantities given in tables 2 and 3 were averaged over the

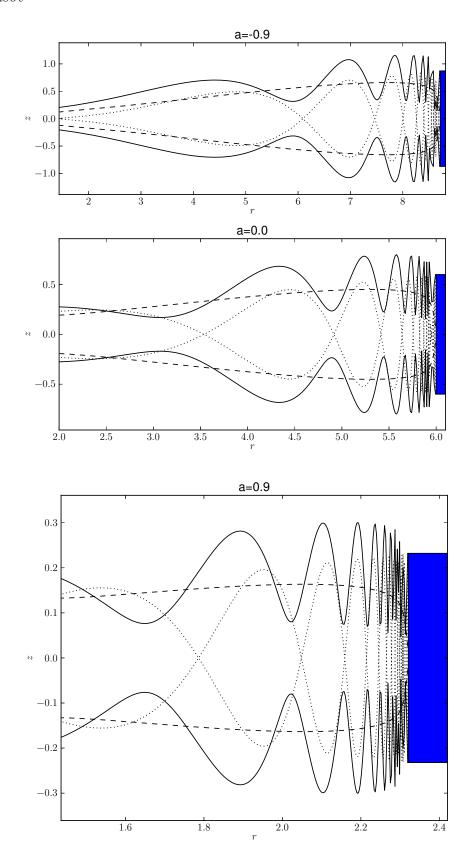


Figure 5. Disc thickness oscillations. Dotted lines show test particle trajectories in absence of pressure (with self-intersections), dashed lines mark the equilibrium disc thickness, and solid lines show magnetically supported disc thickness dynamical evolution. The bars on the right show schematically the initial thickness of the disc. Initial disc thickness everywhere is set to $h_0 = 0.1$.

time ranges (given in table 1 for every model) when accretion was relatively stable.

5.2 Results and comparison to analytical estimates

5.2.1 Overview

Main simulation results are given in tables 2 and 3. Animations based on the results are available on *YouTube*, and the raw data may be provided upon request.

Evolution of the magnetized torus follows more or less a single scenario: first, the parts of magnetic loops extending beyond the torus rapidly expand and straighten because in these parts the plasma is nearly force-free. Inside the disc, magnetic fields are frozen-in and evolve slowly, mainly due to differential rotation and magneto-rotational instability (MRI, see Balbus & Hawley (1991)). After thousands of dynamical times, magnetic field amplification saturates, and quasi-steady accretion establishes. The saturated magnetic fields are strongly anisotropic with $B^{\hat{\varphi}} \gg B^{\hat{r}}$ but this may be an artifact of 2D approach. Three-dimensional numerical simulations such as Fromang & Papaloizou (2007); Parkin & Bicknell (2013) suggest that saturated chaotic magnetic fields in accretion discs with Keplerian rotation are indeed anisotropic but with the toroidal fields about one-two orders of magnitude stronger, not two-three orders as twodimensional simulations predict. Such a discrepancy is not unexpected. As the large-scale vertical magnetic field loses its energy due to magneto-rotational instability, the amplitudes of the radial and toroidal fields are determined by the secondary (parasitic) instabilities (Goodman & Xu 1994) of the field configuration formed by the MRI as well as by differential rotation of the flow, Parker instability and reconnections (Tout & Pringle 1992). Parker instability in axisymmetric approximation is unable to affect the strength of toroidal magnetic field, while in 3D it may easily bend magnetic field lines in vertical direction and thus transfer azimuthal magnetic fields into vertical.

For most of the simulations, toroidal fields are strong enough to determine the inner flow structure. In table 3, the larger value of the two equilibrium thicknesses (determined by initially toroidal or initially radial fields) is relevant as an estimate for the expected thickness of a magnetically supported disc.

In the multiple-loop case, complicated magnetic field structure somehow delays rapid field amplification and quasi-stationary accretion establishes later (about 10^4 from the start of the simulation). The start of quasi-stationary accretion regime depends strongly on the starting magnetic field configuration and varies from one run to another by a factor of several.

Viscosity parameter α was calculated as:

$$\alpha = \left\langle \frac{T_{EM}^{\hat{r}\hat{\varphi}}}{p} \right\rangle = \left\langle \sqrt{\frac{g_{rr}}{g_{\varphi\varphi}}} \frac{T_{EM}^{r} \varphi}{p} \right\rangle \tag{23}$$

Averaging was performed near the equatorial plane in the inner part of the accretion torus between r_{ISCO} and $2r_{ISCO}$ (see α_{out} values in table 2) and in the supersonic flow between the last stable orbit and event horizon (α_{in}) .

Viscosity parameter seems to be strongly dependent on coordinates, being about unity inside the ISCO and above the disc surface. I estimated the mean α acting in the flow by averaging the above expression over two disc heights inside the relevant range of radii. Disc height itself was measured according to the technique described in section 5.2.2.

The resultant values of viscosity parameter in the disc are about several percent or less. However, further from the equatorial plane viscous stresses are about the same, while thermal energy density decreases, and α may be, say, an order of magnitude larger if larger distances (about 20°) from the equatorial plane are considered. The viscosity parameter behaviour near ISCO was considered with the help of HARM in the work of Shafee et al. (2008). Their results are qualitatively similar to mine.

For different models, the product $\alpha\beta=\left\langle\frac{2B^{\hat{r}}B^{\varphi}}{B^2}\right\rangle$ varies in the range $0.01\div0.2$. Because azimuthal fields are much stronger, $\alpha\beta\sim\sqrt{\frac{\beta_r}{\beta_\varphi}}$ (the third, vertical magnetic field component is even smaller than the radial). Interpreted in terms of the "tilt angle" $\theta_B=\frac{1}{2}\arcsin(\alpha\beta)$, the estimated values yield $\theta_B\sim0.2\div5^\circ$. Since comprehensive three-dimensional MHD simulations argue for a universal value of $\theta_B\simeq12\div13^\circ$ (Sorathia et al. 2012), we conclude that in real discs the contribution of azimuthal fields should be smaller by a factor of several.

5.2.2 Disc thicknesses

Disc thickness was measured by Gaussian fitting of density distributions with polar angle, averaged within one of the two radial ranges: between one and two ISCO radii and inside the marginally bound orbit with $r_{mb} = 2 - a + 2\sqrt{1 - a}$. Starting with this radius rather than r_{ISCO} allows to ignore the transition region where initial radial velocity and toroidal magnetic fields are important. Importance of the marginally bound orbit is clearly seen in simulations by Abramowicz et al. (2010) where viscous stresses are still dynamically important down to r_{mb} in transonic discs but not further. Vertical density scale in the first region $(1..2)r_{ISCO}$ was taken as an estimate for $h_0 = (H/r)_0$, while in the second $r_{hor}...r_{mb}$ was compared with $h_{eq} = H_{eq}/r$ for the actual span of radial coordinates. For h_0 , the Gaussian σ for all the models is of the order 0.1 that corresponds to half-width thickness of about 0.2. Thus the disc may be considered reasonably geometrically thin. For the α , β and h_0 values in the simulations, the inner flow should be thinner than the disc itself.

Different vertical scales are compared in figures 6, 8 and 9 for the single-loop case and in figures 10 and 11 for multi-loop configurations. Individual snapshots are also given as examples of density and magnetic field behaviour. Vertical contraction is more profound than one would expect in a magnetically supported disc but is rather stopped by thermal pressure (compare the black solid curve to the green dashed line in the five figures) or even further. However, B1h model suggests that spatial scales smaller than H_m may appear only on coarse meshes but the H_m scale is stable. The H_{eq} spatial scale is in fact present but is better seen if one considers density distribution averaged in time or if mag-

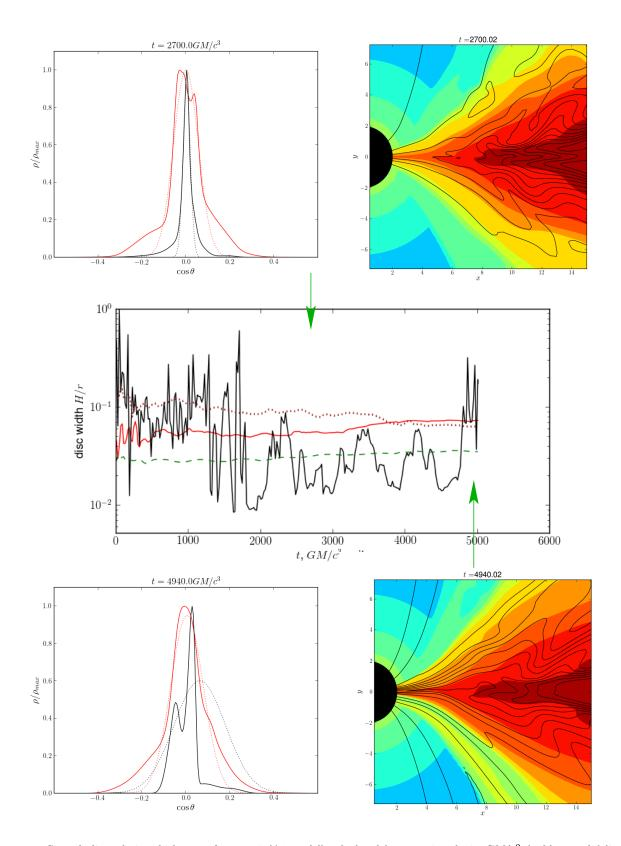


Figure 6. Central: disc relative thicknesses for a=0 (A1 model) calculated between 6 and 12 GM/c^2 (red/grey solid line) and between 2 and 6 GM/c^2 (black solid line). Equilibrium magnetically-supported disc thicknesses calculated for $r=r_{hor}$ (red/grey dotted line) and for $r=r_{ISCO}$ (black dotted) are also shown. Green dashed curve shows the estimated equilibrium thickness of a disc supported by thermal pressure (at $r=r_{mb}$). Upper and lower right panels show two representative snapshots at the instances shown by the arrows. Density is shown by colours/shades (logarithmic scale), and magnetic field lines are marked by contours. Corresponding radially-integrated density profiles are shown in the corresponding left panels: inner region $(r_{hor}..r_{mb})$ is shown with a black solid curve, disc region $(r_{hor}..r_{mb})$ with a red/grey solid curve. Dotted curves are Gaussian approximations.

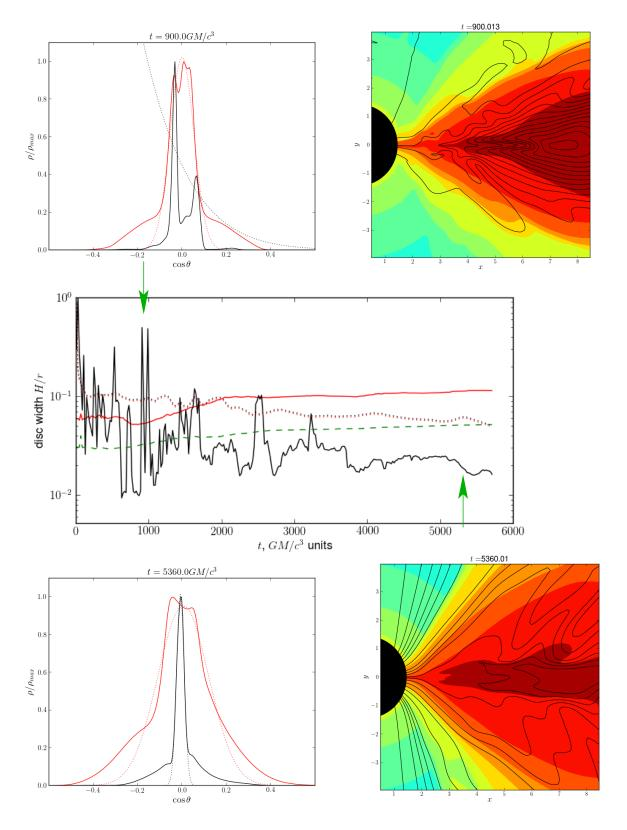


Figure 7. Same as previous figure, but for a = 0.9 (B1 model).

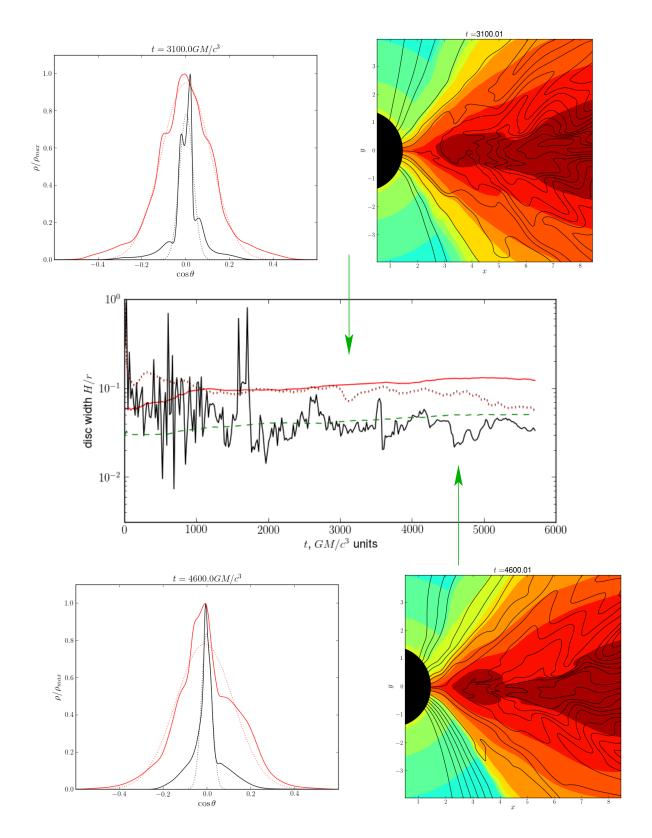


Figure 8. Same as previous figure, but with higher resolution (B1h model, a=0.9).

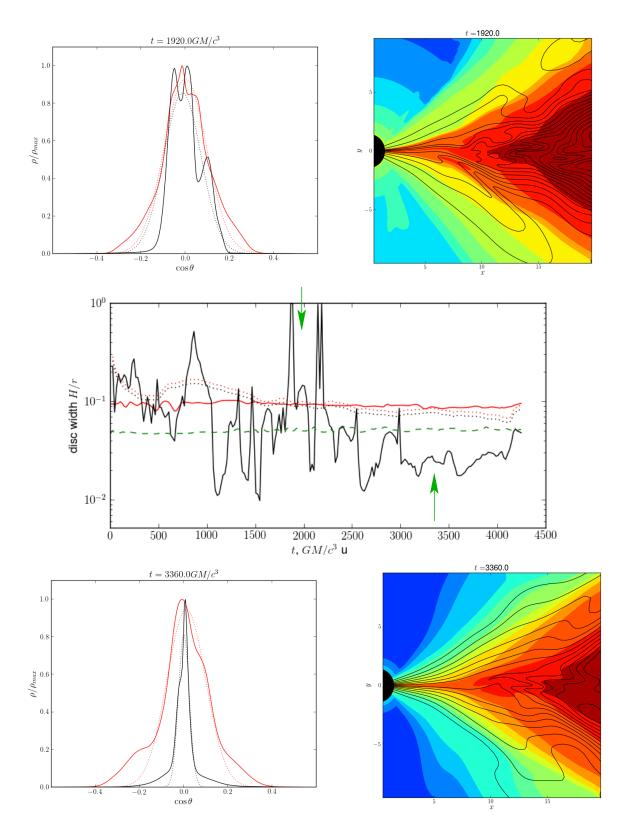


Figure 9. Same as previous figure, but for a = -0.9 (counter-rotation, C1 model).

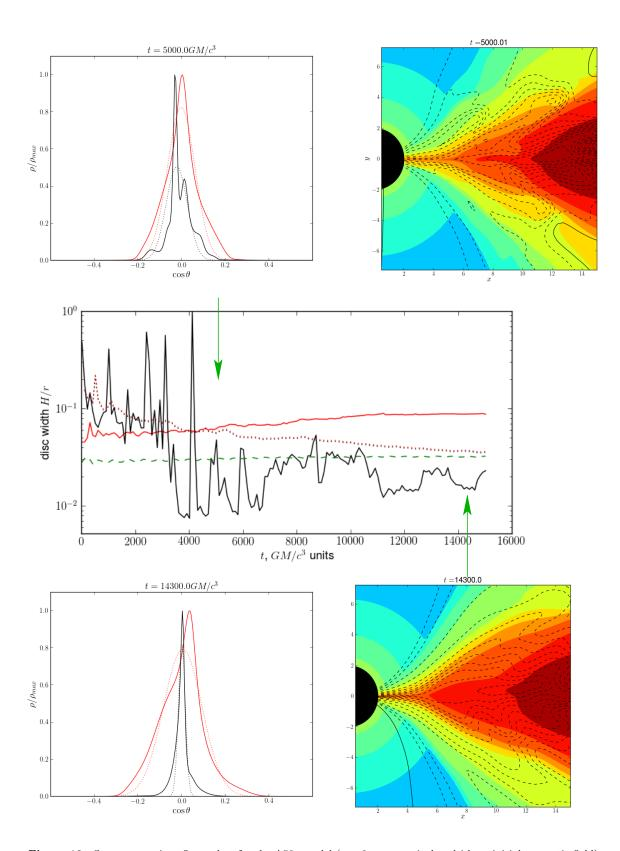


Figure 10. Same as previous figure, but for the A50s model (a = 0, symmetrical multi-loop initial magnetic field).

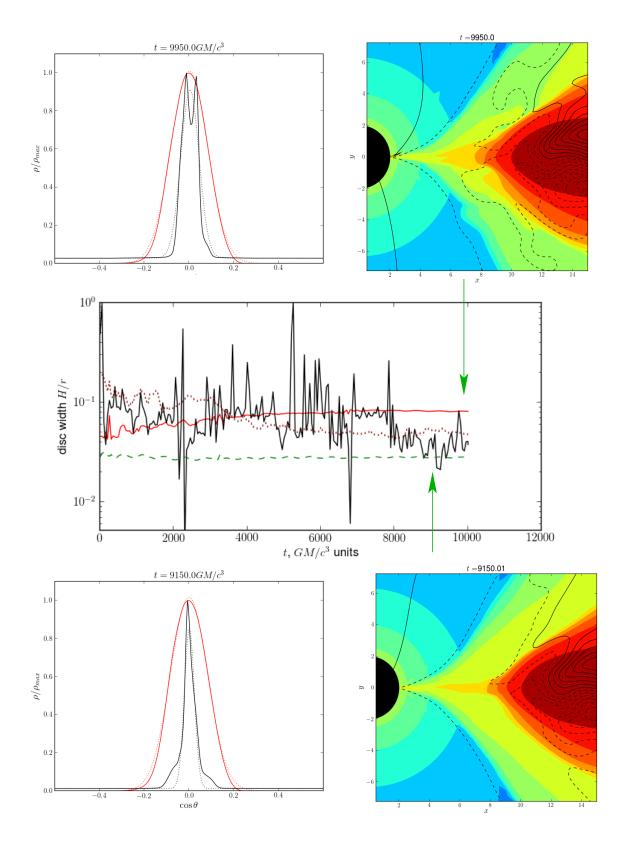


Figure 11. Same as previous figure, but for the A50a model (a = 0, antisymmetric multi-loop initial magnetic field).

Table 1. HARM model parameters. The time ranges (in GM/c^3) used for averaging are also given. Parameters of the initial Fishbone-Moncrief torus, r_{max} (radius of maximal density) and r_{in} (inner radius) are also given.

Model	a	β_{init}	r_{max}	r_{in}	number of loops	time range
A1	0	2000	15.0	9.5	1	2000-5000
B1	0.9	2000	8.4	4.8	1	3000-5700
B1h (192×320)	0.9	2000	8.4	4.8	1	2000-5700
C1	-0.9	2000	19.7	12.8	1	2500 - 4500
A50s	0	2000	19.7	12.8	50	10000-15000
A50a	0	2000	19.7	12.8	50	8000-10000

Table 2. HARM simulation results. The values of α and β in the disc and inside the ISCO are given. Uncertainties are in fact root mean square deviations and reflect primarily the temporal variability of the quantities.

Model	$lpha_{out}$	$lpha_{in}$	eta_r	eta_{arphi}
A1	$0.035 {\pm} 0.016$	$0.5 {\pm} 0.5$	3000 ± 3000	$2.6 {\pm} 0.6$
B1	$0.0085 {\pm} 0.0010$	$0.034 {\pm} 0.007$	24000 ± 10000	5.1 ± 0.6
B1h	0.010 ± 0.003	0.020 ± 0.014	$(1 \pm 0.8) \times 10^4$	3.1 ± 0.8
C1	0.047 ± 0.005	$0.5 {\pm} 0.2$	2000 ± 300	3.9 ± 1.2
A50s	$0.012 {\pm} 0.002$	$0.16 {\pm} 0.07$	$(5 \pm 2) \times 10^4$	1.09 ± 0.09
A50a	0.00165 ± 0.0002	0.04 ± 0.05	$(2.0 \pm 0.4) \times 10^5$	5.3 ± 0.3

netic stresses are considered rather than densities. In figure 12, vertical structure averaged over time and radii between $r_{hor}..r_{mb}$ is shown for thermal pressure and vertical (T_z^z) magnetic stress component. Magnetic stress seems to vary on spatial scales close to H_{eq} apart from H_m . The pressure maximum also becomes broader after averaging because the positions of the very narrow $(H \sim 0.01)$ maxima in the free-falling flow vary with time. Sometimes, even two or more such streams are present separated by distances closer either to the initial disc thickness or to the H_{eq} scale dictated by magnetic field stresses.

In the multi-loop case, there is as well no general consistence with the estimated flow vertical scale and predictions of the analytical model. Symmetric and antisymmetric models behave similarly. Finer structure connected to individual loops and current sheets is seen in individual slices even better (see figures 10 and 11)

It seems that the MHD flow is in fact unstable to the processes that split the flow into thin streams with lower magnetization supported by thermal pressure rather than magnetic fields, sandwiched into a thicker magnetized layer with the vertical scale of about H_{eq} . Since magnetic field changes direction (see figure 12), the structure of the flow may be characterised as a driven current sheet. Reconnections in this current sheet may be one of the sources of energy released inside the ISCO. The spatial scales of the current sheets, however, may be beyond the scope of MHD approach. For example, the "thin current sheets" in terrestrial magnetosphere have thicknesses of the order of ion gyro-radii (Zelenyi et al. 2011), the spatial scale that MHD approach can not reveal since it does not account for the masses of the particles and existence of different particle populations.

The observed inflow structure has much in common with the non-linear MRI solution found by Goodman & Xu (1994) for the case of extreme compressibility. In this solution, the medium is vertically stratified into regions with different horizontal field direction divided by thin dense layers of compressed matter that exists near the nodes of

horizontal magnetic field. Such a solution emerges if magnetic field tension becomes much stronger than thermal pressure that is indeed the case for the flow inside the ISCO. There is usually only one radial field alternation in the inner flow, probably because the vertical scale of a magnetically supported disc essentially coincides by the order of magnitude with the wavelength of the fastest-growing MRI mode $\lambda_{MRI} \sim 2\pi v_{Az}/\Omega_z$.

6 DISCUSSION

6.1 Observability of the inner flow

As it was mentioned in the Introduction, the inner flow receives enough power to become comparable in its luminosity to the accretion disc itself. The question is whether the flow is cooled efficiently enough to emit significant part of this power. Compton cooling time is likely less than the free-falling time (see for example Di Matteo et al. (1997)):

$$t_C \sim \frac{1}{l_S} \frac{GM}{c^3} \sim \frac{m_e}{m_p} \frac{1}{l_{Edd}\Theta} \times \frac{GM}{c^3},$$

where $\Theta=kT/m_ec^2$ and $l_S=\frac{r}{L}\frac{\sigma_T}{m_ec^3}$ is seed photon compactness. The above formula assumes $r\sim GM/c^2$ and $L\sim l_{Edd}\frac{4\pi GMm_p}{c\varkappa},\ l_{Edd}$ is Eddington ratio. Dimensionless temperature may be estimated by considering the balance of heating and cooling mechanisms as $\Theta\sim 0.1\tau\left(L_H/L_S\right)^{1/4}\sim 0.1$ (see Pietrini & Krolik (1995)) where $L_{H,S}$ are heating and seed photon luminosities, and τ is scattering optical depth in the inner flow.

The inner flow is cooled efficiently by inverse Compton losses since its temperature is about tens of keV and luminosity is determined by the thermal and possibly magnetic energy stored inside the disc (see Introduction). Hence the inner flow is a probable candidate for the source of X-ray

Table 3. Disc thicknesses estimated in the HARM simulations. Uncertainties are in fact root mean square deviations and reflect primarily the temporal variability of the quantities. Disc thicknesses given in this table are calculated for the two intervals, one outside and one inside ISCO, and compared to the magnetically supported relative disc thickness near horizon and to the pressure supported disc thickness estimated for r_{mb} .

Model	$(1-2)r_{ISCO}$	$r_{hor}-r_{mb}$	$\frac{H_{eq}}{r}(r_{hor})$		$\frac{H_m}{r}(r_{mb})$
			radial	toroidal	
A1	0.064 ± 0.008	0.04 ± 0.04	0.078 ± 0.011	0.20 ± 0.03	0.034 ± 0.002
B1	0.108 ± 0.005	0.025 ± 0.007	0.063 ± 0.004	0.025 ± 0.003	0.049 ± 0.002
B1h	0.118 ± 0.012	0.040 ± 0.011	$0.089 {\pm} 0.0014$	0.029 ± 0.003	$0.047 {\pm} 0.004$
C1	0.090 ± 0.003	0.030 ± 0.13	0.073 ± 0.004	0.36 ± 0.03	$0.0525 {\pm} 0.0015$
A50s	$0.086 {\pm} 0.004$	0.023 ± 0.008	0.040 ± 0.004	$0.41 {\pm} 0.01$	$0.0324 {\pm} 0.003$
A50a	0.082 ± 0.006	0.040 ± 0.011	0.050 ± 0.003	0.43 ± 0.03	0.0283 ± 0.0003

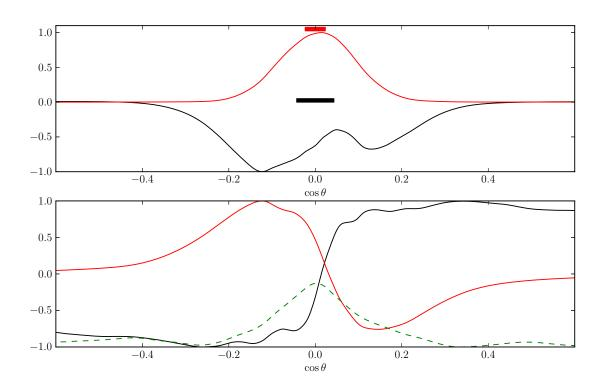


Figure 12. Vertical structure of the free-falling flow averaged in time (2000..5700) and in the radial range of $r_{hor}..r_{ISCO}$, model B1h. In the upper panel, thermal pressure (red/grey) and electromagnetic stress component $-T_z^z$ are shown together with the bars representing the estimated thickness scales H_m/r (red/grey) and H_{eq}/r (black) at r_{mb} . Lower panel shows similarly averaged magnetic field components: $B^{\hat{r}}$ (solid black), B^z (dashed green) and toroidal $B^{\hat{\varphi}}$ (solid red/grey).

radiation of quasars that is known to emerge from a region of the size $\sim r_{ISCO}$. The characteristic X-ray luminosities of QSO are about 0.01-0.1 of their bolometric luminosities (Runnoe et al. 2012), and the X-ray spectrum is generally consistent with non-saturated Comptonization.

6.2 Limitations of the model

If the inner flow scatters a large number of seed photons (produced in the disc or near the last stable orbit), it will also experience radiation drag. I suppose that this effect is essentially unimportant for angular momentum transport because the angular momenta of matter and radiation leav-

ing the last stable orbit are more or less the same. However, if rotation parameter becomes close to the Thorne's critical value of $a \simeq 0.998$ (Thorne 1974), photons with lower angular momenta will enter the regions close to the black hole more often. On the other hand, photons with larger angular momenta may spend more time on grazing orbits. These effects are probably subtle unless Kerr parameter is high.

Another possible effect that may alter the radial structure of the inner flow is angular momentum transfer by non-diagonal terms in electromagnetic stress-energy tensor. If these terms are important, estimate (1) for the radial velocity needs to be replaced by more comprehensive dynamical equations. Besides, specific energy and angular momentum

may now vary with radius. Magnetic field will be important in angular momentum transfer if its contribution to stress-energy tensor becomes comparable to that of in-falling matter. Condition that magnetic field effects are *small* in the weakly magnetized flow is:

$$\frac{B^r B^{\varphi}}{4\pi \rho u^r u^{\varphi}} < 1,$$

where ρ is the rest mass density of the (cold, non-relativistic in sense of its temperature) in-falling matter. Both velocity components are moderately relativistic $u^r \sim u^\varphi \sim 1,$ and $\rho \sim \frac{\dot{M}}{4\pi H r u^r}.$ Taking into account equipartition in the disc (equation (12)), magnetic field tension component may be roughly estimated as:

$$\frac{B^r B^\varphi}{4\pi} \sim B_0^2 \times \frac{1}{4\pi} \left(\frac{H_0 r_0}{H r}\right)^2 \sim \frac{\dot{M} v_K^0}{4\pi\alpha\beta H_0 r_0} \left(\frac{H_0 r_0}{H r}\right)^2$$

Hence:

$$\frac{B^r B^\varphi}{4\pi \rho u^r u^\varphi} \sim \frac{1}{\alpha\beta} v_K^0 u^r \frac{H_0 r_0}{H r} \sim \frac{H_0 r_0}{H r} \sim \frac{1}{\alpha\beta} \frac{H_0 r_0}{H r}$$

If $H=H_{eq}$ (equations (19-21)), the above condition may be re-written as:

$$\left(\frac{H_0}{\alpha\beta}\right)^{2/3} \frac{r_0}{r} \lesssim 1 \tag{24}$$

This condition is easily fulfilled for thin discs if $\alpha\beta\gtrsim 1$ and $H_0\lesssim 1$. It may still hold even if $\alpha\beta\lesssim 1$ but for accretion discs thin enough. The model becomes invalid for $h_0\gtrsim \alpha\beta$ for one more reason illustrated by the empirical scalings (19-21). If the relative disc thickness is larger than $\alpha\beta$, the inner flow is geometrically thick and the expressions for the radial gravity become incorrect. Geometry of the flow may also change qualitatively if it becomes thicker. In particular, some part of it may escape to infinity forming a jet or some other type of an outflow.

6.3 Conclusions

I conclude that the flow inside the last stable orbit should have a disc-like structure with the vertical spatial scale $\sim \left(\frac{h_0}{\alpha\beta}\right)^{1/3}$. Numerical simulations support existence of similar vertical scales but the flow actually has a more complicated vertical structure, possibly containing single or multiple thinner layers (or streams, in 3D) supported by thermal pressure rather than magnetic stresses. The reason is probably that the magnetically supported flow is unstable and the turbulent magnetic field configuration has the tendency to collapse into current sheets with less-magnetized interior supported in vertical direction by thermal pressure rather than magnetic fields.

ACKNOWLEDGMENTS

The author would like to thank Alexander Tchekhovskoy for his help with HARM, Kirill Sokolovsky for providing

me with additional computational resources, and the referee (Chris Reynolds) for drawing my attention towards the MHD instabilities operating in the magnetized flow. I also acknowledge support from the Dynasty Foundation and from the RFBR grant 14-02-91172 GFEN_a.

REFERENCES

Abolmasov P., 2013, MNRAS, 432, 761

Abramowicz M. A., Jaroszyński M., Kato S., Lasota J.-P., Różańska A., Sądowski A., 2010, A&A, 521, A15

Abramowicz M. A., Lanza A., Percival M. J., 1997, ApJ, 479, 179

Balbus S. A., Hawley J. F., 1991, ApJ, 376, 214

Batygin V. V., Toptygin I. N., 1978, Problems in Electrodynamics: Second Edition. Academic Press

Beskin V., Tchekhovskoy A., 2005, A&A, 433, 619

Blandford R. D., Znajek R. L., 1977, MNRAS, 179, 433

Boyer R. H., Lindquist R. W., 1967, Journal of Mathematical Physics, $8,\,265$

Chen B., Dai X., Baron E., Kantowski R., 2013, ApJ, 769, 131

Chen B., Dai X., Kochanek C. S., Chartas G., Blackburne J. A., Kozłowski S., 2011, ApJL, 740, L34

Di Matteo T., Blackman E. G., Fabian A. C., 1997, MN-RAS, 291, L23

Fishbone L. G., Moncrief V., 1976, ApJ, 207, 962

Fromang S., Papaloizou J., 2007, A&A, 476, 1113

Gammie C. F., McKinney J. C., Tóth G., 2003, ApJ, 589, 444

Goodman J., Xu G., 1994, ApJ, 432, 213

Komissarov S. S., 2006, MNRAS, 368, 993

Krolik J. H., 1999, ApJL, 515, L73

Landau L. D., Lifshitz E. M., 1971, The classical theory of fields. Pergamon International Library of Science, Technology, Engineering and Social Studies, Oxford: Pergamon Press, 1971, 3rd rev. engl. edition

Morgan C. W., Hainline L. J., Chen B., Tewes M., Kochanek C. S., Dai X., Kozlowski S., Blackburne J. A., Mosquera A. M., Chartas G., Courbin F., Meylan G., 2012, ApJ, 756, 52

Noble S. C., Gammie C. F., McKinney J. C., Del Zanna L., 2006, ApJ, 641, 626

Parkin E. R., Bicknell G. V., 2013, MNRAS, 435, 2281

Penna R. F., McKinney J. C., Narayan R., Tchekhovskoy A., Shafee R., McClintock J. E., 2010, MNRAS, 408, 752 Pietrini P., Krolik J. H., 1995, ApJ, 447, 526

Runnoe J. C., Brotherton M. S., Shang Z., 2012, MNRAS, 422, 478

Shafee R., McKinney J. C., Narayan R., Tchekhovskoy A., Gammie C. F., McClintock J. E., 2008, ApJL, 687, L25

Shakura N. I., Sunyaev R. A., 1973, A&A, 24, 337

Shapiro S. L., Teukolsky S. A., 1983, Black holes, white dwarfs, and neutron stars: The physics of compact objects. Research supported by the National Science Foundation. New York, Wiley-Interscience, 1983, 663 p.

Sorathia K. A., Reynolds C. S., Stone J. M., Beckwith K., 2012, ApJ, 749, 189

Thorne K. S., 1974, ApJ, 191, 507

Tout C. A., Pringle J. E., 1992, MNRAS, 259, 604

Zelenyi L. M., Malova H. V., Artemyev A. V., Popov V. Y., Petrukovich A. A., 2011, Plasma Physics Reports, 37, 118 Zhu Y., Davis S. W., Narayan R., Kulkarni A. K., Penna R. F., McClintock J. E., 2012, MNRAS, 424, 2504